

Predictive Inorganic Synthesis based on Machine Learning using Small Data sets: a case study of size-controlled Cu Nanoparticles

Brent Motmans,^{1, 2, 3, 4} Digvijay Ghogare,^{5, 3, 4, 6} Thijs G.I. van Wijk,^{1, 3} An Hardy,^{5, 3, 4} and Danny E.P. Vanpoucke^{1, 3}

¹ Hasselt University, Institute for Materials Research (*imo-imomoc*),

Quantum & Artificial inTelligence design Of Materials (*QuATOMs*), Martelarenlaan 42, B-3500 Hasselt, Belgium

² Hasselt University, Institute for Materials Research (*imo-imomoc*),

Hybrid Materials Design (*HyMaD*), Martelarenlaan 42, B-3500 Hasselt, Belgium

³imec, *imo-imomoc*, Wetenschapsspark 1, B-3590 Diepenbeek, Belgium

⁴Energyville, *imo-imomoc*, Thor Park 8320, B-3600 Genk, Belgium

⁵ Hasselt University, Institute for Materials Research (*imo-imomoc*),

Design and Synthesis of Inorganic Materials (*DESINE*), Martelarenlaan 42, B-3500 Hasselt, Belgium

⁶Electrochemistry Excellence Centre (*ELEC*), Materials & Chemistry Unit,

Flemish Institute for Technological Research (*VITO*), Boeretang 200, Mol, 2400 Belgium

(Dated: December 19, 2025)

Copper nanoparticles (Cu NPs) have a broad applicability, yet their synthesis is sensitive to subtle changes in reaction parameters. This sensitivity, combined with the time- and resource-intensive nature of experimental optimization, poses a major challenge in achieving reproducible and size-controlled synthesis. While Machine Learning (ML) shows promise in materials research, its application is often limited by scarcity of large high-quality experimental data sets. This study explores ML to predict the size of Cu NPs from microwave-assisted polyol synthesis using a small data set of 25 in-house performed syntheses. Latin Hypercube Sampling is used to efficiently cover the parameter space while creating the experimental data set. Ensemble regression models, built with the AMADEUS framework,[1, 2] successfully predict particle sizes with high accuracy ($R^2 = 0.74$), outperforming classical statistical approaches ($R^2 = 0.60$). Overall, this study highlights that, for lab-scale synthesis optimization, high-quality small datasets combined with classical, interpretable ML models outperform traditional statistical methods and are fully sufficient for quantitative synthesis prediction. This approach provides a sustainable and experimentally realistic pathway toward data-driven inorganic synthesis design.

1. INTRODUCTION

Metal nanoparticles (NPs) play a central role in a broad range of applications, including catalysis, electronics, and biomedicine, due to their unique size- and shape-dependent properties.[3–6] However, controlling these properties requires very precise control of various NP characteristics, including their morphology (*i.e.*, size and shape), composition, and surface chemistry down to the nanometer scale. Achieving this level of control remains one of the biggest challenges in NP synthesis, as small variations in the synthesis can lead to final particles with entirely different properties.[5, 7] Traditionally, synthesis optimization relies on iterative, empirical approaches that are slow, resource-intensive, and often lack mechanistic insight.[7] To overcome these limitations, more systematic, data-driven strategies are needed, and recent advances in artificial intelligence (AI) and machine learning (ML) offer promising opportunities to accelerate the development of reproducible and tailored NP syntheses.[7–13]

By uncovering hidden correlations in complex parameter spaces, ML can guide experimental design and reduce the number of required experiments.[9–12] In materials science, ML is now routinely used to uncover the structure–property relationships of materials, thereby accelerating the discovery of new materials with specific properties.[9–12] However, for synthesis optimization,

the key challenge lies in predicting how synthesis parameters determine the resulting crystal structure or particle morphology. These synthesis–structure relationships are far less explored, yet crucial for rational synthesis design. As a result, recent data-driven approaches are shifting towards models that learn synthesis–structure relationships to accelerate synthesis optimization.[13–15] Unlike traditional one-variable-at-a-time (OVAT) approaches, which are slow and fail to capture the multidimensional correlations that govern synthesis outcomes, ML can account for such interactions and thereby accelerate synthesis optimization.[15, 16] However, while large data sets underpin many ML successes [17–19], they are rarely feasible in laboratory-scale chemistry, where the creation of each data point requires a significant amount of time and resources. In the specific case of inorganic NP synthesis, literature-based data sets are often inconsistent and biased, as failed experiments remain unpublished[20–22], as shown by Huo *et al.*[17], who expected up to 16% of the values to be incorrect. As such, robust ML workflows for small, high-quality data sets often remain underexplored.

ML can identify which synthesis parameters most strongly influence inorganic NP outcomes, as demonstrated by Guda *et al.*[23], who trained ML models on 30 data points to classify the results of gold NP synthesis (success, shape, and formation kinetics) based on the precursor concentrations, reducing agent, and surfactant. ML also enables closed-loop experimentation,

where ML models suggest subsequent experiments based on previous results, accelerating optimization and supporting high-throughput synthesis.[24, 25] Pellegrino *et al.*[26] trained neural networks (NNs), with 20 initial data points, to predict the size, dispersion, and aspect ratio of TiO_2 NP, identifying optimal synthesis parameters through reverse engineering. Similarly, Williams *et al.*[27] combined Design of Experiments (DoE) and random forests to accurately predict the yield of Ag nanowires in a polyol-based flow reactor, based on 31 samples.

In the current work, the prediction of copper (Cu) NP size as function of synthesis parameters is explored. Cu NPs hold significant promise for various catalytic processes, such as electro-catalysis and photo-catalysis, due to their abundance, cost-effectiveness, and versatile properties.[5, 28, 29] For example, Reske *et al.*[29] showed that decreasing the size of Cu NPs significantly improves their catalytic activity. Different synthesis methods give rise to different types of Cu NPs, which may differ in particle size, morphology, and extent of oxidation. While metallic Cu NPs are nominally (Cu^0), they often undergo (partial) surface oxidation depending on the synthesis conditions, leading to (CuO_x) phases of varying composition.[5] The wide variety of possible synthesis outcomes, as well as the large parameter space, complicates the development of robust synthesis procedures to obtain specific properties.

Though ML is a tool with great potential for Cu NP synthesis, two challenges need to be tackled. The first challenge is finding a good quality data set to train the ML model, as a model can only be as good as its training data.[20–22] To tackle this challenge, a consistent and qualitative data set is built in-house. The second challenge is overcoming the data hungry nature of typical ML methods. Since the goal is to make synthesis optimization more efficient using ML, it makes no sense to first conduct hundreds of experiments that can serve as data to train the model. Therefore, a small data set of only a few experiments is used.[2, 14] Finally, within the context of lab-scale experiments, we emphasize interpretable ML: the model should not only predict outcomes, but also provide insight into the role of different synthesis parameters.

In this work, we develop an interpretable ML model for Cu NP synthesis based on a small, high-quality data set, aiming to accelerate synthesis optimization while providing fundamental insights into parameter effects. In addition, performance of the interpretable ML model is also compared with the more classical DoE approach.

2. METHODOLOGY

Within this work, we follow a four step workflow (Figure 1), of which the latter three can form a closed-loop experimentation methodology. The initial set of parameters for the data set is selected using Latin Hyper-

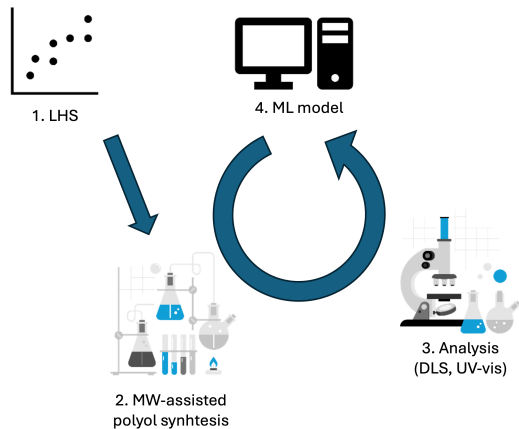


Figure 1: Visualization of the workflow followed to create the data set and model the syntheses.

cube Sampling (LHS) to achieve optimal parameter space coverage.[30] The sampled syntheses are performed in the lab via MW-assisted polyol synthesis. The resulting dispersions are analyzed via dynamic light scattering (DLS) to determine the particle size of the Cu NPs, while the surface plasmon resonance (SPR) peak is determined using UV-Vis measurements. The effective synthesis parameters[31] and corresponding particle sizes are combined into the data set for the ML modeling. In a closed-loop approach, the results of the ML models can be used to assist in further experimental syntheses, or further validation of the ML model.

2.1. Experimental synthesis

1. Materials

For all experimental syntheses, absolute ethanol ($\geq 99.8\%$ analytical grade) obtained from Fisher Chemical and copper(II) acetate monohydrate ($\text{Cu}(\text{OAc})_2 \cdot \text{H}_2\text{O}$, ACS reagent), tetramethylammonium hydroxide (TMAH, 25 wt. % in H_2O) and ethylene glycol ($\geq 99\%$) obtained from Sigma Aldrich are used. All reagents are used as received without further purification.

2. Sampling synthesis parameters

LHS is used to obtain an optimized data set with minimal correlation between the various experiments while providing an optimal coverage of the parameter space under investigation.[30, 32, 33] In this work, the parameter space comprises three dimensions:

1. Cu precursor concentration (1 mM to 10 mM)
2. Reaction time (1 minute to 20 minutes)
3. Reaction temperature (175 °C to 200 °C)

Using LHS, 25 experiments are selected that fill this parameter space as optimally as possible.

3. Cu NPs synthesis

The Cu NPs are synthesized via the microwave (MW)-assisted polyol route[32, 34–37] in a CEM Discover SP MW reactor. First, the amount of Cu(OAc)₂ is weighed into the reaction vial. It is then dissolved in 5 ml of ethylene glycol under sonication. After the Cu precursor has completely dissolved, the tetramethylammonium hydroxide (TMAH) is added to the solution and further mixed and degassed under sonication. TMAH is consistently used at a molar ratio of 4 : 1 relative to the Cu precursor. The reaction vessel is then placed in the microwave reactor, with the head space filled with inert argon up to a pressure of 5 bar, and is first stirred for 2 minutes at 80°C to ensure complete dissolution of the precursor. Afterwards, the temperature is raised to the desired reaction temperature with continuous stirring and maintained for the desired reaction time. After the reaction time has passed, the reaction is quenched by actively cooling the vessel with compressed air. A brown-red suspension is obtained, which is typical for Cu NPs.[35] To collect the Cu NPs, the reaction mixture is diluted with 15 ml of ethanol and centrifuged at 11000 rpm for 10 minutes. Subsequently, the supernatant is removed, and the resulting NPs are again dispersed in 20 ml of ethanol.

4. Characterization

The SPR of the synthesized Cu NPs in the ethylene glycol dispersion is determined by UV-Vis measurements with the Agilent Cary 5000 spectrophotometer equipped with a dual-beam configuration. Measurements are performed in a quartz cuvette (10 mm path length) over a wavelength range of 300–800 nm. Baseline correction is applied using the ethylene glycol solvent as reference.

The size of the synthesized Cu NPs is determined as the hydrodynamic diameter via DLS measurements with a Zetasizer Nano ZS, equipped with a 633 nm He-Ne laser. For these measurements, the ethanolic Cu dispersions are sonicated for at least 10 minutes. Subsequently, five drops of the NP dispersion are diluted with ethanol to a total volume of approximately 2–3 mL, ensuring the disposable polystyrene cuvette is filled above the required optical path.

2.2. Computational modeling

Two modeling tasks are performed on the data set: a regression task based on ensemble regression ML, implemented in the AMADEUS framework,[1, 2] and these

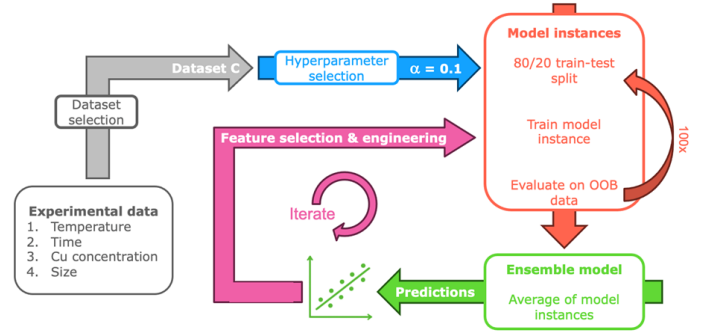


Figure 2: The computational modeling starts with selecting the best performing data set. Next, the optimal value for the regularization strength α is selected. Then, 100 model instances are trained on random subsets of the data set. From these an ensemble model is created through averaging over all instances. Finally, through an iterative application of feature engineering and selection next generation models are created.

results are compared with classical DoE[38], to gain insight in the potential of ML.

1. Ensemble regression models

Since ML using small data sets is very sensitive to the selected training data, and hyperparameter tuning suffers from this volatility[2, 14], we make use of the scikit-learn-based AMADEUS framework which was designed to deal with small data sets (Figure 2).[1, 2, 14, 39] Pasting-type ensemble models consisting of 100 base instances are created, using either linear or polynomial base models in combination with LASSO regularization.[40] Each of the instances is trained on a different randomly selected 80/20 split (in-bag/out-of-bag (OOB)) of the complete data set. The resulting final ensemble model is a single base instance equal to the average of the 100 base model instances.

To determine and compare the accuracy and generalization of the various models, root-mean-squared error (RMSE), mean absolute error (MAE) and coefficient of determination (R^2) are used as performance metrics. These errors can be determined on the in-bag and OOB data, with the difference between the two providing an indicator on model overfitting, while the individual values of the OOB error are quality indicators of the models' generalization. A low training error and high OOB error are very strong indicators of a model that is overfitting. The average model quality (MAE, RMSE and R^2) is determined by having the final ensemble model make predictions for all data points in the entire data set, and correlates very well with the OOB quality measure.

We first examine the impact of multi-modal data in our dataset. For this purpose, three data sets are created:

1. Data set A: All 25 data points are included in the

data set, and the predicted particle size is the smallest particle size present in the DLS particle-size distribution.

2. Data set B: All 25 data points are included in the data set, and the predicted particle size corresponds to the peak with the highest percentage contribution in the DLS particle-size distribution.
3. Data set C: Only the 18 data points with a mono-modal DLS particle-size distribution are included in the data set.

For each of these data sets, ensembles of polynomial regression models of order 1 to 5 with LASSO regularization ($\alpha = 1.0$) are trained. The performance metrics of the best performing ensemble model are presented in Table I, and show that data set C performs significantly better. Therefore, only data set C will be considered further. The trained models in this study thus focus on predicting the particle size for a mono-modal distribution (cf. SI Figures 9, 10 and 11) and therefore cannot predict situations where a multi-modal distribution is obtained.

When using a small data set, the growing number of features in polynomial models quickly leads to overfitting. Because the hyperparameter tuning of the regularization strength α (LASSO regularization) presented itself to be too volatile for automatic optimization, it is selected based on visual comparison of four values ($\alpha = 1.0, 0.1, 0.01$, and 0.001). Ensemble models with polynomials up to degree eight as base model are trained. Analysis of the ensemble model MAE shows an overall optimal performance for $\alpha = 0.1$ (cf. SI Figure 5). Furthermore, the hyperparameter behavior shows no further improvement above polynomial degree three. Therefore, no features above degree three are considered, further reducing overfitting.

A further measure employed to reduce overfitting, is consideration of what one could call ensemble importance.[14, 41] The AMADEUS framework tracks how often a polynomial feature is retained (*i.e.* has non-zero coefficient) within the ensemble, after regularization of the features in each of the model instances. This provides a measure of importance of the features with regard to a well-generalizing model. A feature with an ensemble importance of 100% has a non-zero coefficient in all model instances in the ensemble. If a feature has an ensemble importance of 75%, this means that in 25% of the model instances in the ensemble, the coefficient for this feature is zero. Based on the trends in ensemble importance, seven features are selected (cf. SI Figure 6):

Table I: Performance metrics of the best-performing ensemble model for the different data sets.

	polynomial degree	RMSE [nm]	MAE [nm]	R^2
Data set A	3	63.46	50.50	0.42
Data set B	3	59.44	46.06	0.35
Data set C	3	34.09	24.28	0.73

1. $[Cu]$
2. T
3. $time$
4. $[Cu]^2$
5. $[Cu]^3$
6. $[Cu] \times T$
7. $[Cu] \times time$

Since $[Cu]$, T , and $time$ are the base parameters used during synthesis, they are all retained as features. $[Cu]^2$ and $[Cu]^3$ are included as they play relatively important roles in both the second and third degree models. The interaction terms $[Cu] \times T$ and $[Cu] \times time$ are included, given their high importance in the second-degree polynomial; higher-order interaction terms are not included to limit model complexity and the probability of overfitting. Using these features, a linear regression model is trained, and iteratively, features are further engineered to obtain the optimal feature set.

2. Classical statistical methods (DoE)

Using DoE[38] software JMP Pro (SAS Institute Inc.), a linear regression model is fitted for data set C, including terms up to the second degree. Insignificant terms are removed until only significant terms remain. In contrast to machine learning approaches, the available data set is not split into training and test data; all data points are used to fit the regression model. The performance of the model is determined by calculating the expected size for all data points using the equation obtained, and thus should be compared to quality estimates on the in-bag data set.

3. RESULTS AND DISCUSSION

3.1. Cu NP syntheses

The DLS measurements show a peak above 5000 nm for five samples. However, these peaks are not included in the analysis. Due to their very low intensity ($< 1.5\%$), it can be assumed that these results are due to contamination, such as dust particles, during the measurements. The synthesis yields Cu NPs with a particle size between 40 nm and 350 nm. The DLS shows a bi-modal and tri-modal particle-size distribution for five and two samples, respectively. The remaining samples show a mono-modal particle-size distribution. Analysis of the DLS intensity-size plots allows us to identify the smallest particle size present. The median of these particle sizes is 157.9 nm over all samples.

Based on the SPR location, the effective formation of Cu metal (Cu^0) NPs is verified for the different samples. The different UV-Vis spectra show a clear SPR peak between 590 nm and 630 nm for most samples, which is a strong indication of the presence of Cu^0 NPs.[35] Samples 4, 6, and 19 do not show a clear SPR feature, which may be due to low particle concentration, oxidation[42], or the presence of ultra small particles ($< 5nm$), which

Table II: Performance metrics of different regression model generations.

	# Features	Training		OOB		Average			R^2
		RMSE [nm]	MAE [nm]	RMSE [nm]	MAE [nm]	RMSE [nm]	MAE [nm]		
1st generation	19	22.17	16.05	86.52	68.51	32.64	22.53	0.75	
2nd generation	7	29.40	20.47	51.85	41.36	32.61	22.28	0.75	
3rd generation	11	27.78	19.79	63.66	52.18	33.07	23.35	0.74	
4th generation	6	30.57	22.39	49.90	40.92	33.03	23.81	0.74	
DoE	2	-	-	-	-	40.91	33.54	0.60	

do not exhibit a well-defined SPR; for the other samples, at least some Cu^0 is present. Given the limited yield of the syntheses, no X-ray diffraction measurements could be performed to provide a conclusive answer, but the combination of the red-brown color of the solution and the presence of a clear SPR peak in the UV-Vis spectra strongly indicate that Cu^0 NPs have indeed formed. To validate this conclusion, Selected Area Electron Diffraction analysis is conducted on sample 22 using a transmission electron microscope operated at an accelerating voltage of 120 kV. The resulting diffraction rings are indexed to the face-centered cubic structure of copper, with prominent rings corresponding to the (111), (200), and (220) planes. The primary diffraction rings are assigned the following d -spacings: 2.08 Å for the (111) plane, 1.83 Å for the (200) plane, and 1.29 Å for the (220) plane. These values agree with the standard values for FCC copper (JCPDS card no. 04-0836)[43], confirming the formation of Cu^0 NPs.

3.2. Quantitative size prediction

1. Ensemble regression

Ensemble regression models are created to predict Cu NP size based on the synthesis parameters. Different generations of models are trained to investigate the influence of different features on model performance.

As first generation ensemble model, we consider the complete third-degree polynomial model with LASSO regularization ($\alpha = 0.1$). This model has an R^2 of 0.75, and RMSE and MAE of 32.64 nm and 22.53 nm, respectively. Despite the very good performance of this first generation model, its main disadvantage is the use of an extensive set of 19 features. With our data set consisting of only 18 samples, the risk of overfitting is significant. In addition, a larger feature set results in a more complex model and, therefore, higher computational cost for inference. With this in mind, the following generations are aimed at reducing the model size drastically to improve generalization and reduce computational cost.

In the second generation, the complexity of the model is strongly reduced by using only the seven features ($[Cu]$, $time$, T , $[Cu]^2$, $[Cu]^3$, $[Cu] \times time$, $[Cu] \times T$) selected based on the ensemble importance analysis. The ensemble average shows no significant loss in performance com-

pared to the first generation (*cf.*, Table II), despite the significant reduction in the number of features used. In addition, the training and OOB errors of the ensemble show that the second generation is more generalizable as their difference becomes smaller. The training error of the second generation increases slightly (MAE of 20.47 nm compared to 16.05 nm), while the OOB error decreases drastically (MAE goes from 68.51 nm to 41.36 nm). The smaller difference between training and OOB error indicates that the model is overfitting less and generalizes better.

In the third generation model, the feature set is expanded with four additional features, aimed at the investigation of the influence of non-polynomial features (based on domain knowledge) on the model performance.

1. $e^{[Cu]}$ is added because $[Cu]$ often has a high and consistent ensemble importance in the investigation of different polynomial models where it occurs in higher powers.
2. $\frac{[Cu]}{time}$ can be interpreted as a measure of the amount of cations available per unit of time during the growth of the particles.
3. $\ln([Cu] \times time)$ provides a measure of the total exposure of the reduction medium to Cu ions.
4. $\frac{[time]}{T}$ as a temperature-normalized reaction time. Although this parameter does not represent the classical thermal budget ($time \times T$), it provides a simple heuristic descriptor that captures part of the interplay between time and temperature in a single scalar.

This more complex feature set, gives rise to a slight decline in the performance of the model due to stronger overfitting, leading to poorer generalization. Given the small difference in performance between this and the previous generation, a comprehensive analysis of the ensemble and dominance importance[44, 45] of the features is carried out. Based on this analysis features are selected, aimed at a good balance between sufficient complexity for good predictive quality and a reduced size while retaining good generalization, which resulted in our fourth generation model.

The dominance importance and ensemble importance are considered in an iterative fashion, as done in previous work of one of the authors.[14, 41] An exhaustive set of sub-models are trained, with one, two or three features

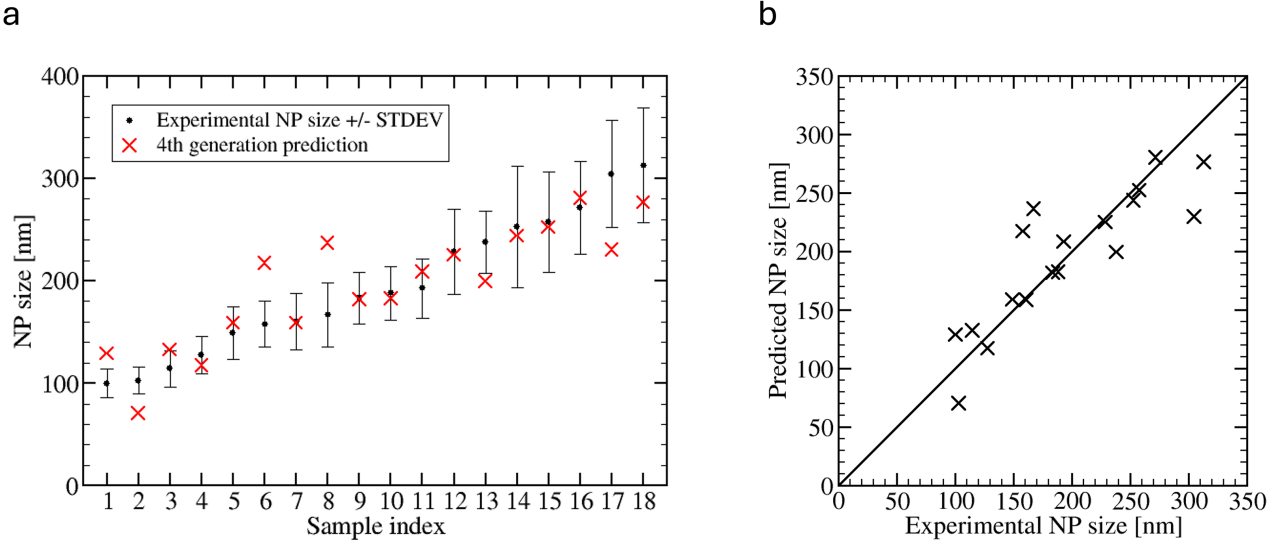


Figure 3: a) Plot of the experimentally measured particle size and their standard deviation in ascending order (black) with the corresponding predicted particle size of the fifth generation ensemble model (red); b) Parity plot of the actual, experimental size against the corresponding predicted size using the fourth generation ensemble model.

(from the full feature list of the third generation model) systematically disabled. This allows us to determine the influence of each individual feature on the model's performance. Five features are found to have a low importance (< 85%) on average over all models. Therefore, only the six features with an average ensemble importance > 90% are kept for the fourth generation (*cf.* SI Table IX).

$$\begin{array}{ll}
 1. T & 4. e^{[Cu]} \\
 2. [Cu] \times \text{time} & 5. \frac{[Cu]}{\text{time}} \\
 3. [Cu]^3 & 6. \ln([Cu] \times \text{time})
 \end{array}$$

The predicted particle sizes resulting from our fourth generation ensemble regression model are shown in figure 3. In this model, each of the six features has an ensemble importance of $\geq 98.0\%$ (LASSO regularization, $\alpha = 0.1$). The quality of the model is only very slightly below the 19-feature model, showing a significant improvement with respect to overfitting (*cf.* Table II). Because the size of the model has been greatly reduced, the MAE for the OOB predictions decreases from 52.18 nm for the third generation to 40.92 nm for the fourth generation, a marked improvement. Since the average of the ensemble model is equivalent to a single model instance with averaged coefficients [2], our fourth generation model can be formulated as follows:

$$\begin{aligned}
 \text{Cu NP size} = & 194.66 - 12.59T - 36.16[Cu]t \\
 & - 123.47[Cu]^3 + 108.12e^{[Cu]} \\
 & + \frac{32.30[Cu]}{t} + 63.00 \ln([Cu]t) \quad (1)
 \end{aligned}$$

In Equation 1, all feature values are standardized prior to training, meaning the coefficients apply to standard-

ized inputs (*cf.* SI Table X). When standardized experimental feature values are inserted into Equation 1, the model directly returns the predicted particle size in nm.

$$\begin{aligned}
 \text{Cu NP size} = & -4.60 \times 10^4 - 1.56T - 9.73 \times 10^2[Cu]t \\
 & - 5.64 \times 10^8[Cu]^3 + 4.66 \times 10^4e^{[Cu]} \\
 & + \frac{3.49 \times 10^4[Cu]}{t} + 68.46 \ln([Cu]t) \quad (2)
 \end{aligned}$$

Equation 2 gives the non-standardized form of the fourth generation model. Here, $[Cu]$ in molar, time in minutes and T in $^{\circ}\text{C}$ can be used directly to obtain the particle size in nm.

2. Statistical approach (DoE)

In the classical statistical approach, only the concentration of the Cu precursor appears to significantly influence the particle size, resulting in a quadratic model shown in figure 4 and given by Equation 3. Here, $[Cu]$ refers to the non-standardized precursor concentration in molar units, and the equation returns the Cu NP size directly in nm. As seen in Table II the quality is significantly lower than the ML regression models. In addition, it is unclear whether the model will generalize successfully, as it is based on the entire data set.

$$\begin{aligned}
 \text{Cu NP size} = & -63.24 + 106542.95[Cu] \\
 & - 8801229.71[Cu]^2 \quad (3)
 \end{aligned}$$

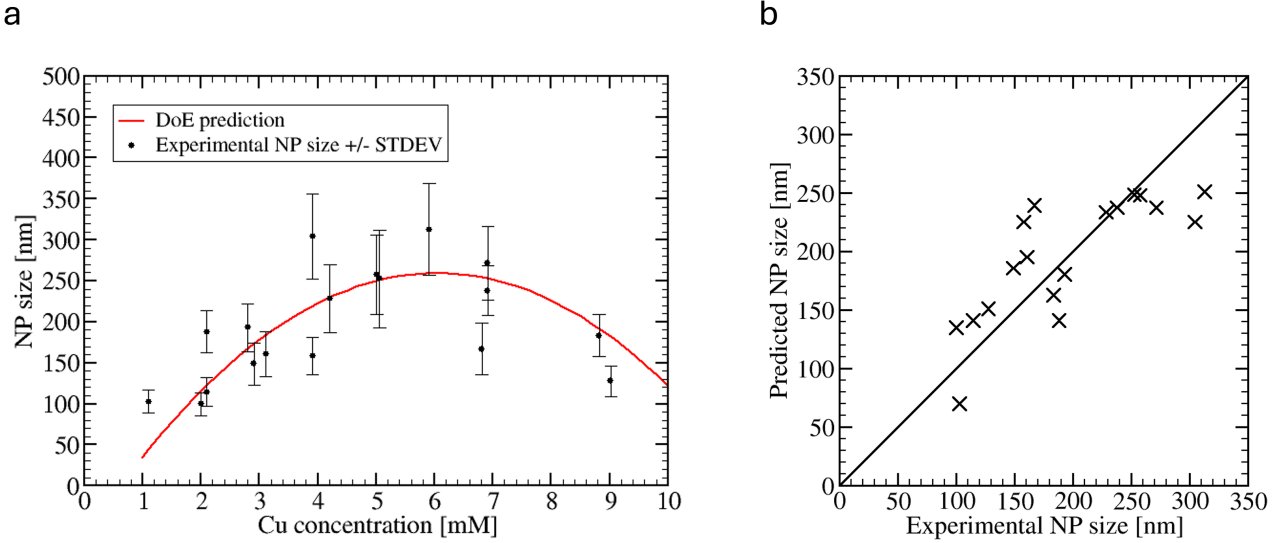


Figure 4: a) Plot of the experimental measured particle sizes and their standard deviation (black) and the statistical model (red); b) Parity plot of the actual, experimental size against the corresponding predicted size using the statistical model.

Since the ensemble regression models are built on random subsets of the entire data set, it can be expected that they will generalize better than the classical regression model that was trained on the entire data set. Because individual data points have a large impact in small datasets, models trained on the full dataset are highly sensitive to noise and outliers. Training multiple model instances on random subsets and averaging their predictions reduces this sensitivity, yielding more accurate and robust models.[2, 14] On the other hand, the classical regression model consists of only two terms containing the precursor concentration, compared to the six features in the ensemble regression model, which results in a simpler model and therefore lower computational cost. Comparison of the ML and DoE models indicates that Cu concentration is an important factor, as both contain it as a polynomial term. In addition, the influence of time and temperature are of relevance as well (as known from experiment) which is captured by the ML models only.

Since the DoE model only retained two features, we attempted to further reduce the fourth generation model by removal of additional features, based on dominance importance analyses (*cf.* SI Table XI). First $\frac{[Cu]}{time}$ was removed, resulting in a slight performance reduction. R^2 dropped from 0.74 to 0.72 and the average MAE increased from 23.81 nm to 25.10 nm. On the OOB data, both models have almost the same MAE, so despite the slightly lower performance there is no increase in generalization. Next, also $[Cu] \times time$ was removed, as it was assumed to be covered by the $\ln([Cu] \times time)$ feature. Now the overall performance further dropped with an R^2 of 0.69 and an average MAE of 27.14 nm. In this case, generalization does increase significantly with

a training MAE of 26.26 nm and an OOB MAE of 36.69 nm. Finally, also $\ln([Cu] \times time)$ was removed from the feature list, to arrive at a three feature model. Again, the generalization of the model increases with a training MAE of 26.56 nm and an OOB MAE of 32.85 nm, while maintaining similar average model performance with an R^2 of 0.69 and an average MAE of 26.96 nm.

This demonstrates the delicate balance between average model performance and overall model generalization. Reducing model size does give significant improvements in generalization, but comes with a cost in average performance. While the fourth generation model with six features had an average MAE of only 23.81 nm, this increased to 26.96 nm for the three feature model, getting closer to the 33.54 nm MAE of the two feature DoE model.

Table III: Comparison of targeted particle sizes, obtained particle sizes and their STDEV from predicted syntheses routes with the fourth generation ensemble model and predicted particle sizes using the DoE model.

Sample	Targeted [nm]	Obtained [nm]	DoE prediction [nm]
26	115	70.78 (± 4.68)	162.67
27	115	117.90 (± 32.06)	153.30
28	220	235.60 (± 34.57)	220.86
29	220	128.60 (± 49.54)	225.19
30	275	165.10 (± 41.04)	251.43
31	275	189.60 (± 59.50)	250.39

3. Synthesis prediction: model validation

For three different target sizes (115 nm, 220 nm and 275 nm) Equation 2 is used to suggest two possible syntheses routes for each (*cf.* SI Table XII). The suggested syntheses are performed using the same experimental procedure used for creating the original data set samples. For two of the targeted particle sizes one of the suggested syntheses routes closely matched the target size within experimental uncertainty (*cf.* samples 27 & 28 in Table III). For the largest particles (samples 30 & 31) neither suggested set of parameters gave the expected results. It is interesting to note that for the incorrect results, the particles are always too small. The suggested synthesis are also used to predict particle size using the DoE model (Equation 3). This shows that the DoE model exhibits a flatter, less pronounced curvature in the explored parameter space compared to the ML model.

4. CONCLUSION

Despite the small size of the data set, it is possible to predict the particle size of Cu NPs quantitatively based on synthesis parameters using classical ensemble regression ML, achieving an R^2 of 0.74 and an MAE of 23.81 nm. For most data points, the predicted particle size falls within the experimental standard deviation. We were able to reduce the number of features in our final model

to six, which improved generalization and reduced model size.

By in-house constructing a consistent data set, we overcome limitations associated with biased or incomplete literature data. The use of interpretable models allowed us to identify the synthesis parameters with the strongest influence on particle properties, providing fundamental insights alongside predictive power. As validation, the final model is used to suggest synthesis routes for specific target particle sizes. For two of the three target sizes, the suggested syntheses closely matched the experimental results, demonstrating that ML can effectively guide experimental synthesis even with a minimal data set.

Although this work focused on Cu NPs as a model system, the approach is broadly applicable to other materials. Future work could integrate such ML workflows into closed-loop experimentation and explore larger, more diverse data sets. Overall, this strategy contributes to more efficient, interpretable, and sustainable materials development.

ACKNOWLEDGMENT

The computational resources and services used in this work were provided by the VSC (Flemish Supercomputer Center), funded by the Research Foundation Flanders (FWO) and the Flemish Government–department WEWIS.

- [1] D. E. P. Vanpoucke, Amadeus v0.2, <https://github.com/DannyVanpoucke/Amadeus> (2020).
- [2] D. E. P. Vanpoucke, O. S. J. van Knippenberg, K. Hermans, K. V. Bernaerts, and S. Mehrkanoon, Small data materials design with machine learning: When the average model knows best, *J. Appl. Phys.* **128**, 054901 (2020).
- [3] M. Daniel and D. Astruc, Gold Nanoparticles: Assembly, Supramolecular Chemistry, Quantum-Size-Related Properties, and Applications Toward Biology, Catalysis, and Nanotechnology, *ChemInform* **35**, 10.1002/chin.200416213 (2004).
- [4] T. Zhai, L. Li, X. Wang, X. Fang, Y. Bando, and D. Goldberg, Recent Developments in One-Dimensional Inorganic Nanostructures for Photodetectors, *Adv. Funct. Mater.* **20**, 4233 (2010).
- [5] M. B. Gawande, A. Goswami, F.-X. Felpin, T. Asefa, X. Huang, R. Silva, X. Zou, R. Zboril, and R. S. Varma, Cu and Cu-Based Nanoparticles: Synthesis and Applications in Catalysis, *Chem. Rev.* **116**, 3722 (2016).
- [6] Q. A. Pankhurst, J. Connolly, S. K. Jones, and J. Dobson, Applications of magnetic nanoparticles in biomedicine, *Phys. D: Appl. Phys.* **36**, R167 (2003).
- [7] N. Baig, I. Kammakakam, and W. Falath, Nanomaterials: a review of synthesis methods, properties, recent progress, and challenges, *Mater. Adv.* **2**, 1821 (2021).
- [8] Z. J. Baum, X. Yu, P. Y. Ayala, Y. Zhao, S. P. Watkins, and Q. Zhou, Artificial Intelligence in Chemistry: Current Trends and Future Directions, *J. Chem. Inf. Model.* **61**, 3197 (2021).
- [9] K. T. Butler, D. W. Davies, H. Cartwright, O. Isayev, and A. Walsh, Machine learning for molecular and materials science, *Nature* **559**, 547 (2018).
- [10] J. Schmidt, M. R. G. Marques, S. Botti, and M. A. L. Marques, Recent advances and applications of machine learning in solid-state materials science, *npj Comput Mater* **5**, 83 (2019).
- [11] B. Sanchez-Lengeling and A. Aspuru-Guzik, Inverse molecular design using machine learning: Generative models for matter engineering, *Science* **361**, 360 (2018).
- [12] G. Huang, Y. Guo, Y. Chen, and Z. Nie, Application of Machine Learning in Material Synthesis and Property Prediction, *Materials* **16**, 5977 (2023).
- [13] A. Agrawal and A. Choudhary, Perspective: Materials informatics and big data: Realization of the “fourth paradigm” of science in materials science, *APL Materials* **4**, 053208 (2016).
- [14] D. E. P. Vanpoucke, M. A. F. Delgove, J. Stouten, J. Nordanijk, N. De Vos, K. Matthysen, G. G. P. Deroover, S. Mehrkanoon, and K. V. Bernaerts, A machine learning approach for the design of hyperbranched polymeric dispersing agents based on aliphatic polyesters

for radiation-curable inks, *Polym Int* **71**, 966 (2022), <https://doi.org/10.1002/pi.6378>.

[15] E. M. Williamson and R. L. Brutchey, Using Data-Driven Learning to Predict and Control the Outcomes of Inorganic Materials Synthesis, *Inorg. Chem.* **62**, 16251 (2023).

[16] N. A. C. Lah, Properties optimisation of nanostructures via machine learning: Progress and perspective, *Engineering Analysis with Boundary Elements* **171**, 106063 (2024).

[17] H. Huo, C. J. Bartel, T. He, A. Trewartha, A. Dunn, B. Ouyang, A. Jain, and G. Ceder, Machine-learning rationalization and prediction of solid-state synthesis conditions, *Chem. Mater.* **34**, 7323 (2022).

[18] A. Merchant, S. Batzner, S. S. Schoenholz, M. Aykol, G. Cheon, and E. D. Cubuk, Scaling deep learning for materials discovery, *Nature* **624**, 80 (2023).

[19] S. Curtarolo, G. L. W. Hart, M. B. Nardelli, N. Mingo, S. Sanvito, and O. Levy, The high-throughput highway to computational materials design, *Nature Mater* **12**, 191 (2013).

[20] C. Chen, Y. Zuo, W. Ye, X. Li, Z. Deng, and S. P. Ong, A Critical Review of Machine Learning of Energy Materials, *Adv. Energy Mater.* **10**, 1903242 (2020).

[21] P. Raccuglia, K. C. Elbert, P. D. F. Adler, C. Falk, M. B. Wenny, A. Mollo, M. Zeller, S. A. Friedler, J. Schrier, and A. J. Norquist, Machine-learning-assisted materials discovery using failed experiments, *Nature* **533**, 73 (2016).

[22] Y. Ma, P. Xu, M. Li, X. Ji, W. Zhao, and W. Lu, The mastery of details in the workflow of materials machine learning, *npj Comput Mater* **10**, 141 (2024).

[23] A. A. Guda, M. V. Kirichkov, V. V. Shapovalov, A. I. Muravlev, D. M. Pashkov, S. A. Guda, A. P. Bagliy, S. A. Soldatov, S. V. Chapek, and A. V. Soldatov, Machine Learning Analysis of Reaction Parameters in UV-Mediated Synthesis of Gold Nanoparticles, *J. Phys. Chem. C* **127**, 1097 (2023).

[24] H. Tao, T. Wu, S. Kheiri, M. Aldeghi, A. Aspuru-Guzik, and E. Kumacheva, Self-Driving Platform for Metal Nanoparticle Synthesis: Combining Microfluidics and Machine Learning, *Adv. Funct. Mater.* **31**, 2106725 (2021).

[25] R. W. Epps, M. S. Bowen, A. A. Volk, K. Abdel-Latif, S. Han, K. G. Reyes, A. Amassian, and M. Abolhasani, Artificial Chemist: An Autonomous Quantum Dot Synthesis Bot, *Adv. Mater* **32**, 2001626 (2020).

[26] F. Pellegrino, R. Isopescu, L. Pellutiè, F. Sordello, A. M. Rossi, E. Ortel, G. Martra, V.-D. Hodoroaba, and V. Maurino, Machine learning approach for elucidating and predicting the role of synthesis parameters on the shape and size of TiO₂ nanoparticles, *Sci Rep* **10**, 18910 (2020).

[27] D. F. Williams, N. Rahimi, J. E. Smay, and S. Hemmati, Optimizing silver nanowire synthesis: machine learning improves and predicts yield for a polyol, millifluidic flow reactor, *Appl Nanosci* **13**, 6539 (2023).

[28] X. Guo, C. Hao, G. Jin, H. Zhu, and X. Guo, Copper Nanoparticles on Graphene Support: An Efficient Photocatalyst for Coupling of Nitroaromatics in Visible Light, *Angew. Chem. Int. Ed.* **53**, 1973 (2014).

[29] R. Reske, H. Mistry, F. Behafarid, B. R. Cuenya, and P. Strasser, Particle Size Effects in the Catalytic Electrocatalysis of CO₂ on Cu Nanoparticles, *J. Am. Chem. Soc.* **136**, 6978 (2014).

[30] P. Borisut and A. Nuchitprasittichai, Adaptive Latin Hypercube Sampling for a Surrogate-Based Optimization with Artificial Neural Network, *Processes* **11**, 3232 (2023).

[31] These are the true experimental values corresponding to the LHS.

[32] J. Teichert, T. Doert, and M. Ruck, Mechanisms of the polyol reduction of copper(II) salts depending on the anion type and diol chain length, *Dalton Trans.* **47**, 14085 (2018).

[33] E. J. Braham, R. D. Davidson, M. Al-Hashimi, R. Arróyave, and S. Banerjee, Navigating the design space of inorganic materials synthesis using statistical methods and machine learning, *Dalton Trans.* **49**, 11480 (2020).

[34] F. Fiévet, S. Ammar-Merah, R. Brayner, F. Chau, M. Giraudeau, F. Mammeri, J. Peron, J.-y. Piquemal, L. Sicard, and G. Viau, The polyol process: a unique method for easy access to metal nanoparticles with tailored sizes, shapes and compositions, *Chem. Soc. Rev.* **47**, 5187 (2018).

[35] M. Blosi, S. Albonetti, M. Dondi, C. Martelli, and G. Baldi, Microwave-assisted polyol synthesis of Cu nanoparticles, *J Nanopart Res* **13**, 127 (2010).

[36] K. J. Carroll, J. U. Reveles, M. D. Shultz, S. N. Khanna, and E. E. Carpenter, Preparation of Elemental Cu and Ni Nanoparticles by the Polyol Method: An Experimental and Theoretical Approach, *J. Phys. Chem. C* **115**, 2656 (2011).

[37] M. Torras and A. Roig, Copper Oxide Nanocubes Wrapping Metals by Microwave Synthesis, *Cryst. Growth Des.* **21**, 5027 (2021).

[38] B. Shahriari, K. Swersky, Z. Wang, R. P. Adams, and N. De Freitas, Taking the Human Out of the Loop: A Review of Bayesian Optimization, *Proceedings of the IEEE* **104**, 148 (2015).

[39] P. Fabian, V. Gaël, G. Alexandre, M. Vincent, T. Bertrand, G. Olivier, B. Mathieu, P. Peter, W. Ron, D. Vincent, V. Jake, P. Alexandre, C. David, B. Matthieu, P. Matthieu, and D. Édouard, SciKit-Learn: Machine Learning in Python, *J. Mach. Learn. Res.* **12**, 2825–2830 (2011).

[40] R. Tibshirani, Regression Shrinkage and Selection Via the Lasso, *Journal of the Royal Statistical Society: Series B (Methodological)* **58**, 267 (1996).

[41] P. Verding, D. E. P. Vanpoucke, Y. T. Aksoy, T. Corthouts, M. R. Vetrano, and W. Deferme, Characterization of droplet formation in ultrasonic spray coating: Influence of ink formulation using phase doppler anemometry and machine learning, *Adv. Mater. Technol.* **10.1002/admt.202502104** (2025), [10.1002/admt.202502104](https://doi.org/10.1002/admt.202502104).

[42] M. A. Vargas-Urbano, L. Marín, W. M. Castillo, L. A. Rodríguez, C. Magén, M. Manotas-Albor, J. E. Diosa, and K. Gross, Effect of Ethylene Glycol: Citric Acid Molar Ratio and pH on the Morphology, Vibrational, Optical and Electronic Properties of TiO₂ and CuO Powders Synthesized by Pechini Method, *Materials* **15**, 5266 (2022).

[43] International Centre for Diffraction Data, *PDF-2: Database card No. 04-0836, Copper (Cu), face-centered cubic* (ICDD, Newtown Square, PA, 2001).

[44] R. Azen and D. V. Budescu, The dominance analysis approach for comparing predictors in multiple regression.,

Psychological Methods **8**, 129 (2003).

[45] H. Huo, C. J. Bartel, T. He, A. Trewartha, A. Dunn, B. Ouyang, A. Jain, and G. Ceder, Machine-learning rationalization and prediction of solid-state synthesis conditions, *Chem. Mater.* **34**, 7323 (2022), <https://doi.org/10.1021/acs.chemmater.2c01293>.

SUPPLEMENTAL INFORMATION

Table IV: Sampled synthesis parameters used for the 25 experimental syntheses. (a) Theoretical concentration of Cu(OAc)₂ precursor in 5 ml ethylene glycol in mM; (b) Effective Cu concentration of Cu(OAc)₂ used; (c) Volume of 2.75 M TMAH in H₂O added to 5 ml ethylene glycol in μ l; (d) Time in minutes reaction mixture is kept on defined temperature; (e) Temperature in °C of reaction mixture for defined reaction time.

Sample	Theoretical Cu conc. ^a [mM]	Effective Cu prec. ^b [mM]	TMAH ^c [μ l]	Time ^d [min]	Temp. ^e [°C]
1	5.00	5.06	36.0	8	196
2	4.00	4.21	29.0	4	188
3	3.00	2.91	21.8	6	198
4	2.00	2.00	14.6	7	184
5	9.00	8.82	65.4	4	180
6	3.00	3.11	21.8	1	194
7	10.00	10.22	72.8	9	188
8	9.00	8.82	65.4	16	182
9	3.00	2.80	21.8	17	182
10	7.00	6.91	51.0	20	194
11	7.00	6.81	51.0	14	186
12	6.00	6.01	43.6	10	192
13	8.00	8.31	58.2	12	184
14	1.00	1.10	7.2	15	198
15	2.00	2.10	14.6	10	196
16	4.00	3.91	29.0	18	200
17	4.00	3.91	29.0	14	192
18	8.00	8.31	58.2	5	180
19	2.00	2.10	14.6	17	176
20	8.00	7.91	58.2	11	190
21	6.00	5.91	43.6	7	178
22	7.00	6.91	51.0	3	176
23	9.00	9.02	65.4	13	178
24	6.00	6.11	43.6	19	186
25	5.00	5.01	36.0	2	190

Table V: Data set A containing 25 datapoints with particle size, the smallest size detected by DLS. (a) Effective concentration of Cu(OAc)₂ precursor in 5 ml ethylene glycol in mM; (b) Volume of 2.75 M TMAH in H₂O added to 5 ml ethylene glycol in μ l; (c) Time in minutes reaction mixture is kept on defined temperature; (d) Temperature in °C of reaction mixture for defined reaction time. (e) Size of the NPs and the standard deviation (STDEV) in nm as measured using DLS.

Sample	Effective Cu conc. ^a [mM]	TMAH ^b [μ l]	Time ^c [min]	Temp. ^d [°C]	Size ^e [nm]
1	5.06	36.0	8	196	252.50 (\pm 59.37)
2	4.21	29.0	4	188	228.40 (\pm 41.47)
3	2.91	21.8	6	198	148.80 (\pm 25.56)
4	2.00	14.6	7	184	99.90 (\pm 14.07)
5	8.82	65.4	4	180	183.30 (\pm 25.42)
6	3.11	21.8	1	194	160.70 (\pm 27.62)
7	10.22	72.8	9	188	64.65 (\pm 8.80)
8	8.82	65.4	16	182	40.85 (\pm 5.20)
9	2.80	21.8	17	182	192.90 (\pm 28.88)
10	6.91	51.0	20	194	237.90 (\pm 30.29)
11	6.81	51.0	14	186	167.00 (\pm 31.15)
12	6.01	43.6	10	192	60.10 (\pm 6.88)
13	8.31	58.2	12	184	66.02 (\pm 11.94)
14	1.10	7.2	15	198	102.90 (\pm 13.51)
15	2.10	14.6	10	196	114.40 (\pm 17.64)
16	3.91	29.0	18	200	157.90 (\pm 22.70)
17	3.91	29.0	14	192	304.50 (\pm 52.21)
18	8.31	58.2	5	180	59.09 (\pm 6.13)
19	2.10	14.6	17	176	188.10 (\pm 26.04)
20	7.91	58.2	11	190	50.36 (\pm 8.16)
21	5.91	43.6	7	178	312.90 (\pm 55.82)
22	6.91	51.0	3	176	271.60 (\pm 45.13)
23	9.02	65.4	13	178	127.60 (\pm 18.55)
24	6.11	43.6	19	186	58.69 (\pm 10.61)
25	5.01	36.0	2	190	257.60 (\pm 48.85)

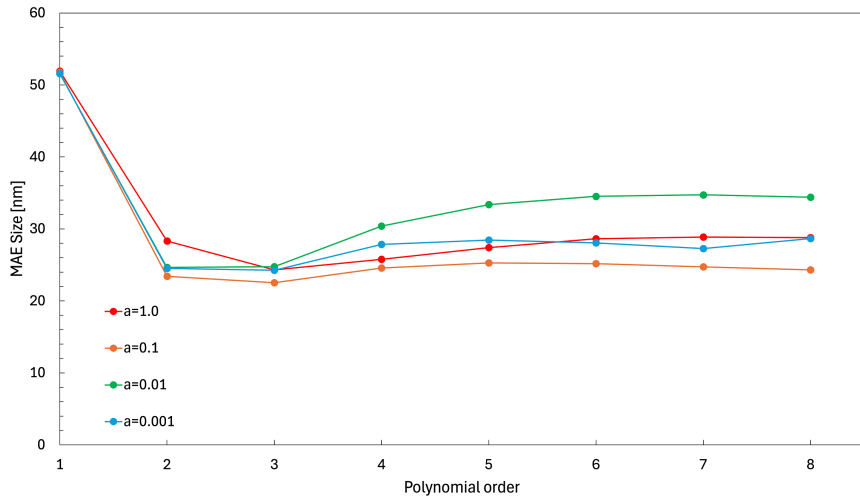


Figure 5: Hyperparameter optimization for size prediction with data set C. LASSO regularized polynomials up to order eight are compared, and MAE of the average ensemble models is shown for $\alpha=1.0$ (red), $\alpha=0.1$ (orange), $\alpha=0.01$ (green), and $\alpha=0.001$ (blue).

Table VI: Data set B containing 25 datapoints with particle size, the size with the highest percentage contribution in DLS. (a) Effective Cu concentration of Cu(OAc)_2 used in 5 ml ethylene glycol; (b) Volume of 2.75 M TMAH in H_2O added to 5 ml ethylene glycol in μl ; (c) Time in minutes reaction mixture is kept on defined temperature; (d) Temperature in $^{\circ}\text{C}$ of reaction mixture for defined reaction time; (e) Size of the NPs and the STDEV in nm as measured using DLS.

Sample	Effective Cu conc. ^a [mM]	TMAH ^b [μl]	Time ^c [min]	Temp. ^d [$^{\circ}\text{C}$]	Size ^e [nm]
1	5.06	36.0	8	196	252.50 (± 59.37)
2	4.21	29.0	4	188	228.40 (± 41.47)
3	2.91	21.8	6	198	148.80 (± 25.56)
4	2.00	14.6	7	184	99.90 (± 14.07)
5	8.82	65.4	4	180	183.30 (± 25.42)
6	3.11	21.8	1	194	160.70 (± 27.62)
7	10.22	72.8	9	188	204.00 (± 34.54)
8	8.82	65.4	16	182	222.30 (± 31.62)
9	2.80	21.8	17	182	192.90 (± 28.88)
10	6.91	51.0	20	194	237.90 (± 30.29)
11	6.81	51.0	14	186	167.00 (± 31.15)
12	6.01	43.6	10	192	269.50 (± 60.33)
13	8.31	58.2	12	184	66.02 (± 11.94)
14	1.10	7.2	15	198	102.90 (± 13.51)
15	2.10	14.6	10	196	114.40 (± 17.64)
16	3.91	29.0	18	200	157.90 (± 22.70)
17	3.91	29.0	14	192	304.50 (± 52.21)
18	8.31	58.2	5	180	184.90 (± 26.97)
19	2.10	14.6	17	176	188.10 (± 26.04)
20	7.91	58.2	11	190	50.36 (± 8.16)
21	5.91	43.6	7	178	312.90 (± 55.82)
22	6.91	51.0	3	176	271.60 (± 45.13)
23	9.02	65.4	13	178	127.60 (± 18.55)
24	6.11	43.6	19	186	58.69 (± 10.61)
25	5.01	36.0	2	190	257.60 (± 48.85)

Table VII: Data set C containing 18 datapoints with monomodal DLS particle-size distribution. (a) Effective Cu concentration of Cu(OAc)_2 used in 5 ml ethylene glycol in mM; (b) Volume of 2.75 M TMAH in H_2O added to 5 ml ethylene glycol in μl ; (c) Time in minutes reaction mixture is kept on defined temperature; (d) Temperature in $^{\circ}\text{C}$ of reaction mixture for defined reaction time; (e) Size of the NPs and the STDEV in nm as measured using DLS.

Sample	Effective Cu conc. ^a [mM]	TMAH ^b [μl]	Time ^c [min]	Temp. ^d [$^{\circ}\text{C}$]	Size ^e [nm]
1	5.06	36.0	8	196	252.50 (± 59.37)
2	4.21	29.0	4	188	228.40 (± 41.47)
3	2.91	21.8	6	198	148.80 (± 25.56)
4	2.00	14.6	7	184	99.90 (± 14.07)
5	8.82	65.4	4	180	183.30 (± 25.42)
6	3.11	21.8	1	194	160.70 (± 27.62)
9	2.80	21.8	17	182	192.90 (± 28.88)
10	6.91	51.0	20	194	237.90 (± 30.29)
11	6.81	51.0	14	186	167.00 (± 31.15)
14	1.10	7.2	15	198	102.90 (± 13.51)
15	2.10	14.6	10	196	114.40 (± 17.64)
16	3.91	29.0	18	200	157.90 (± 22.70)
17	3.91	29.0	14	192	304.50 (± 52.21)
19	2.10	14.6	17	176	188.10 (± 26.04)
21	5.91	43.6	7	178	312.90 (± 55.82)
22	6.91	51.0	3	176	271.60 (± 45.13)
23	9.02	65.4	13	178	127.60 (± 18.55)
25	5.01	36.0	2	190	257.60 (± 48.85)

Table VIII: Resulting sizes and SPR peaks of the different synthesis samples. (a) Hydrodynamic diameter in nm of the Cu NPs and the STDEV measured using DLS in ethanol; (b) Percentage contribution of the respective peak to the DLS particle-size distribution; (c) Due to their irrelevant size and minimal contribution to the DLS particle-size distribution, these peaks will not be considered during the further study; (d) Location of the SPR peak in nm as measured in ethylene glycol using UV-Vis.

Sample	Size_1 ^a [nm]	Percentage_1 ^b [%]	Size_2 ^a [nm]	Percentage_2 ^b [%]	Size_3 ^a [nm]	Percentage_3 ^b [%]	SPR ^d [nm]
1	252.50 (± 59.37)	99.9	5414.00 (± 647.80) ^c	0.1	-	-	613
2	228.40 (± 41.47)	99.9	5135.00 (± 775.60) ^c	0.1	-	-	625
3	148.80 (± 25.56)	100	-	-	-	-	612
4	99.90 (± 14.07)	100	-	-	-	-	699
5	183.30 (± 25.42)	100	-	-	-	-	597
6	160.70 (± 27.62)	100	-	-	-	-	699
7	64.65 (± 8.80)	29.1	204.00 (± 34.54)	70.9	-	-	592
8	40.85 (± 5.20)	33.1	222.30 (± 31.62)	66.9	-	-	590
9	192.90 (± 28.88)	100	-	-	-	-	609
10	237.90 (± 30.29)	100	-	-	-	-	591
11	167.00 (± 31.15)	98.9	5164.00 (± 744.50) ^c	1.1	-	-	636
12	60.10 (± 6.88)	27.1	123.70 (± 22.78)	14.1	269.50 (± 60.33)	-	622
13	66.02 (± 11.94)	53.0	126.20 (± 18.36)	4.7	259.90 (± 45.83)	58.8	611
14	102.90 (± 13.51)	100	-	-	-	-	618
15	114.40 (± 17.64)	100	-	-	-	-	619
16	157.90 (± 22.70)	100	-	-	-	-	593
17	304.50 (± 52.21)	100	-	-	-	-	616
18	59.09 (± 6.13)	30.4	184.90 (± 26.97)	69.6	-	-	605
19	188.10 (± 26.04)	99.7	5532.00 (± 608.70) ^c	0.3	-	-	626
20	50.36 (± 8.16)	63.5	233.10 (± 37.46)	36.5	-	-	595
21	312.90 (± 55.82)	100	-	-	-	-	609
22	271.60 (± 45.13)	99.9	5380.00 (± 654.70) ^c	0.1	-	-	601
23	127.60 (± 18.55)	100	-	-	-	-	595
24	58.69 (± 10.61)	56.4	247.00 (± 39.81)	43.6	-	-	600
25	257.60 (± 48.85)	100	-	-	-	-	597

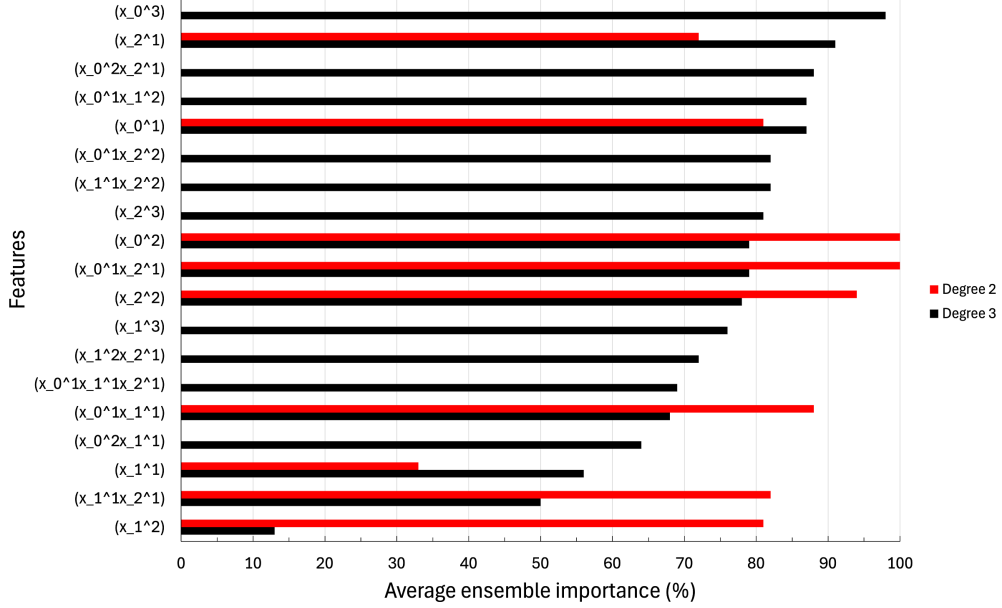


Figure 6: Overview of feature importance, sorted by increasing importance in the third degree polynomial, in the polynomial models with degree two (red) and degree three (black), and trained on data set C with $\alpha=0.1$. $x_0 = \text{Cu}$ precursor concentration, $x_1 = \text{Reaction temperature}$ and $x_2 = \text{Reaction time}$.

Table IX: Summary of the dominance importance analysis performed on the third generation ensemble model.

Feature	Average EI [%]	Minimum EI [%]	Maximum EI [%]
$[Cu]$	84.5	10.0	100
T	99.6	97.0	100
time	82.2	54.0	100
$[Cu]^2$	82.3	53.0	100
$[Cu] \times T$	80.0	43.0	100
$[Cu] \times \text{time}$	99.1	95.0	100
$[Cu]^3$	98.0	85.0	100
$e^{[Cu]}$	91.7	62.0	100
$\frac{[Cu]}{\text{time}}$	95.1	84.0	100
$\ln([Cu] \times \text{time})$	91.9	80.0	100
$\frac{\text{time}}{T}$	84.7	63.0	100

Table X: Mean and standard deviation (STDEV) used to standardize the different features in the 4th generation ensemble model.

Feature	Mean	STDEV
T	1.88×10^2	8.07×10^0
$[Cu] \times \text{time}$	4.42×10^{-2}	3.72×10^{-2}
$[Cu]^3$	1.75×10^{-7}	2.19×10^{-7}
$e^{[Cu]}$	1.00×10^0	2.32×10^{-3}
$\frac{[Cu]}{\text{time}}$	8.90×10^{-4}	9.27×10^{-4}
$\ln([Cu] \times \text{time})$	-3.49×10^0	9.20×10^1

Table XI: Summary of the three best performing models resulting from the dominance importance analysis performed on the fourth generation ensemble model. 1 indicating the feature is included in the model, and 0 indicating the feature is not included.

T	$[Cu] \times \text{time}$	$[Cu]^3$	$e^{[Cu]}$	$\frac{[Cu]}{\text{time}}$	$\ln([Cu] \times \text{time})$	MAE train	MAE OOB	RMSE train	RMSE OOB
1	1	1	1	0	1	24.45	37.69	32.47	45.57
1	0	1	1	0	1	26.21	36.86	34.73	44.36
1	0	1	1	0	0	26.66	34.43	35.33	42.58

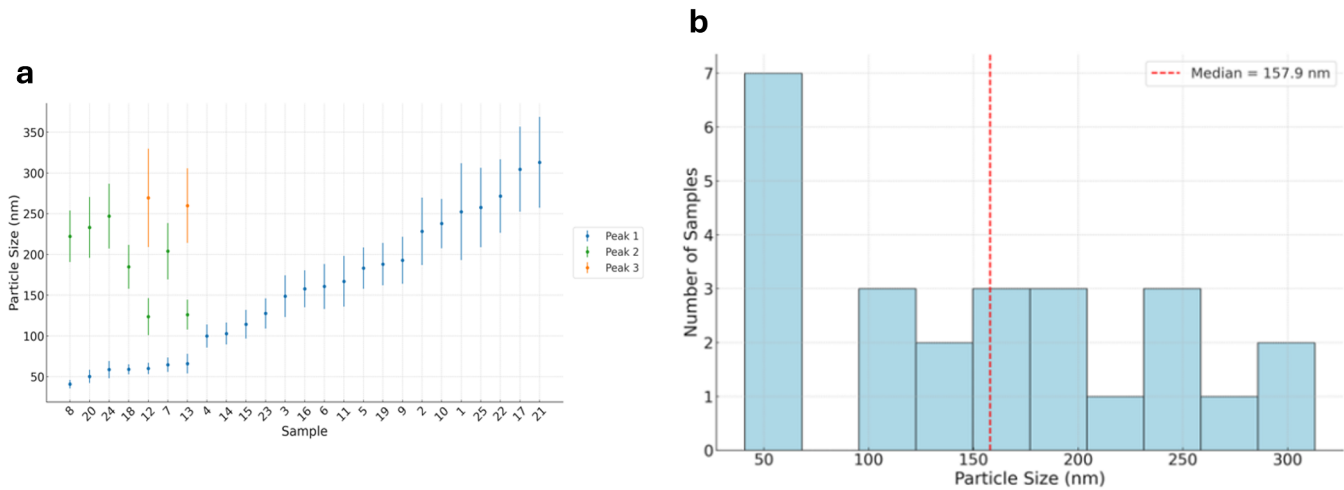


Figure 7: a) DLS results showing particle sizes and standard deviations for all detected peaks per sample. Each point represents a population of a distinct size (Peak 1 in blue, Peak 2 in green, and Peak 3 in orange), with error bars indicating the corresponding standard deviation. Samples are sorted in ascending order based on the size of Peak 1. Peaks above 5000 nm were excluded due to their negligible intensity (<1.5%); b) Distribution of the smallest detected particle size per sample as measured by DLS. The red line indicates the median particle size.

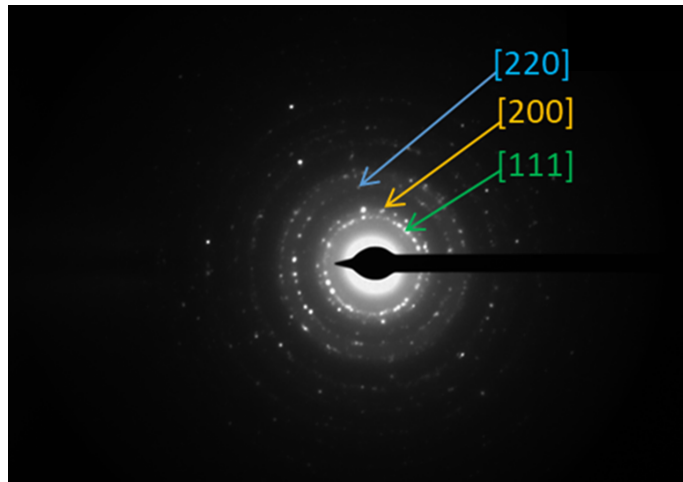


Figure 8: Selected area electron diffraction pattern of Cu^0 nanoparticles from sample 22, recorded at an acceleration voltage of 120 kV. The presence of concentric diffraction rings indicates a polycrystalline material. The rings are indexed to the face-centred cubic (FCC) crystal lattice of metallic copper, with corresponding (111), (200) and (220) planes. The measured d-spacings for these planes are 2.08 Å, 1.83 Å, and 1.29 Å, respectively, in good agreement with standard reference values.

Table XII: Synthesis suggestions made by fourth generation model. (a) Effective concentration of $Cu(OAc)_2$ precursor in 5 ml ethylene glycol in mM; (b) Volume of 2.75 M TMAH in H_2O added to 5 ml ethylene glycol in μl ; (c) Time in minutes reaction mixture is kept on defined temperature; (d) Temperature in °C of reaction mixture for defined reaction time; (e) Targeted hydrodynamic diameter in nm of the Cu NPs measured using DLS in ethanol; (f) Obtained hydrodynamic diameter in nm of the Cu NPs and the STDEV measured using DLS in ethanol.

Sample	Cu conc. ^a [mM]	TMAH ^b [μl]	Time ^c [min]	Temp. ^d [°C]	Targeted size ^e [nm]	Obtained size ^f [nm]
26	8.82	64.0	18	175	115	70.78 (± 4.68)
27	2.30	16.8	4	195	115	117.90 (± 32.06)
28	7.51	54.6	16	175	220	235.60 (± 34.57)
29	3.91	27.8	7	189	220	128.60 (± 49.45)
30	5.51	40.0	15	175	275	165.10 (± 41.04)
31	6.01	43.6	4	179	275	189.60 (± 59.50)

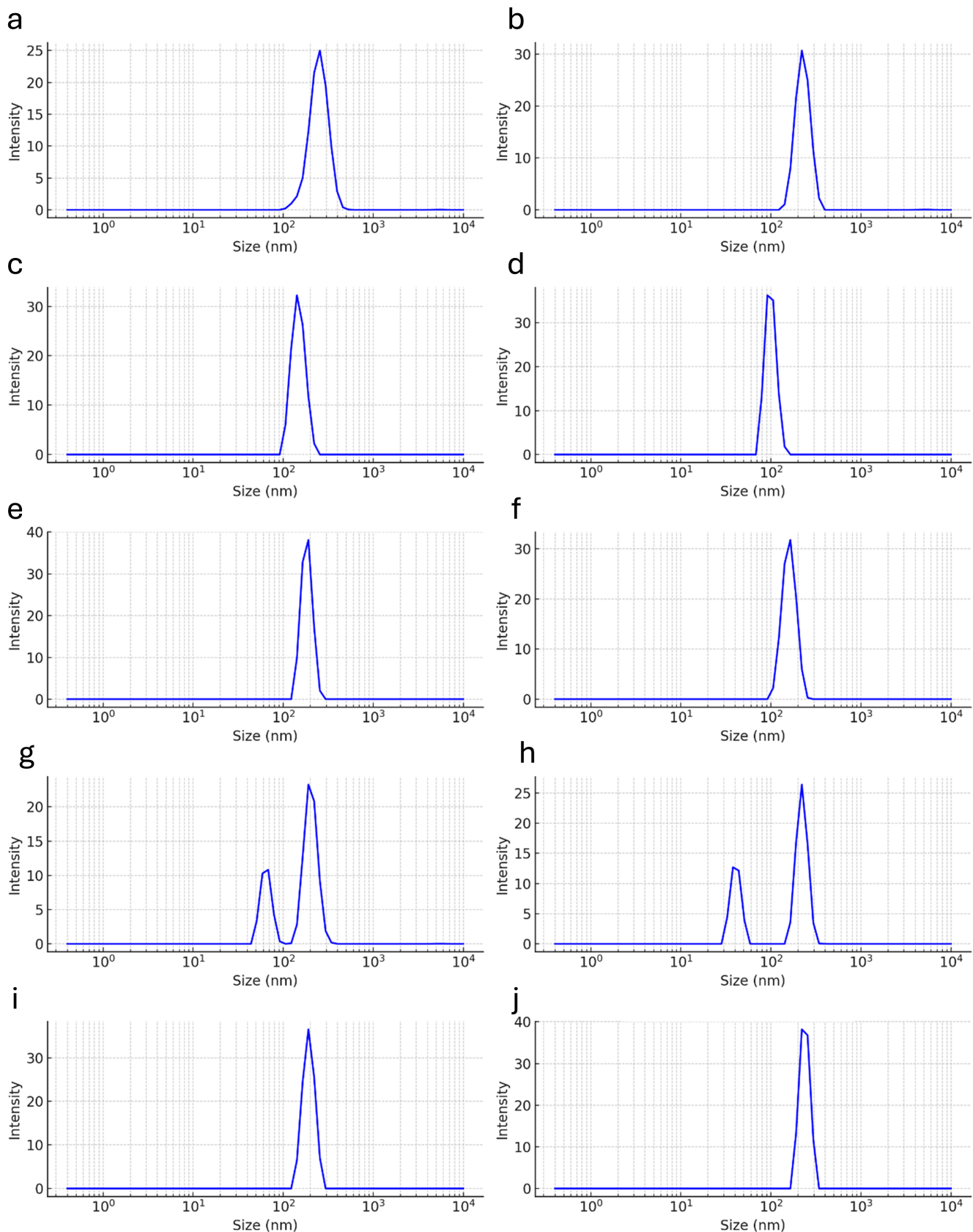


Figure 9: Particle-size distribution resulting from DLS of experimental synthesis a)Sample_1; b)Sample_2; c)Sample_3; d)Sample_4; e)Sample_5; f)Sample_6; g)Sample_7; h)Sample_8; i)Sample_9; j)Sample_10.

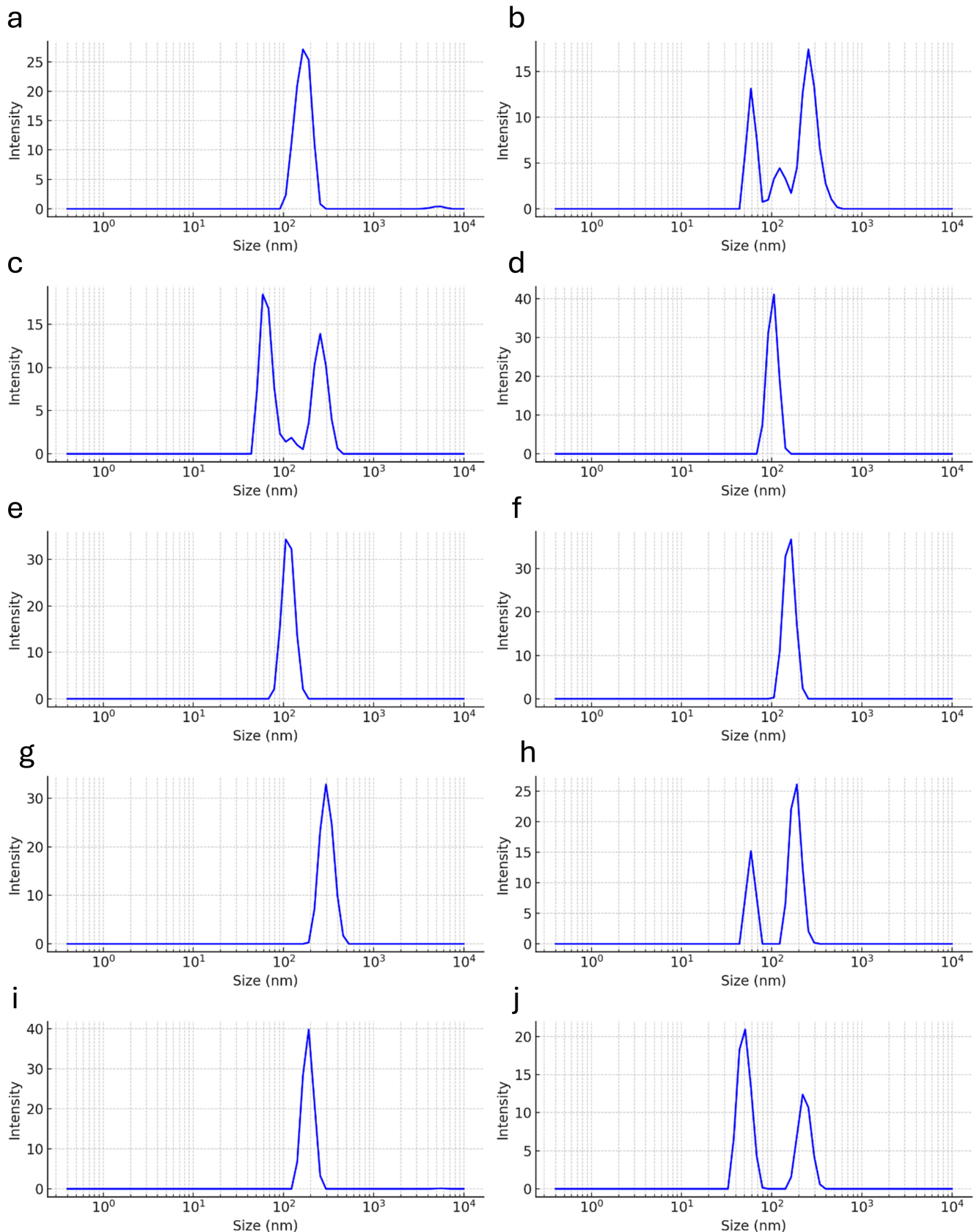


Figure 10: Particle-size distribution resulting from DLS of experimental synthesis a)Sample_11; b)Sample_12; c)Sample_13; d)Sample_14; e)Sample_15; f)Sample_16; g)Sample_17; h)Sample_18; i)Sample_19; j)Sample_20.

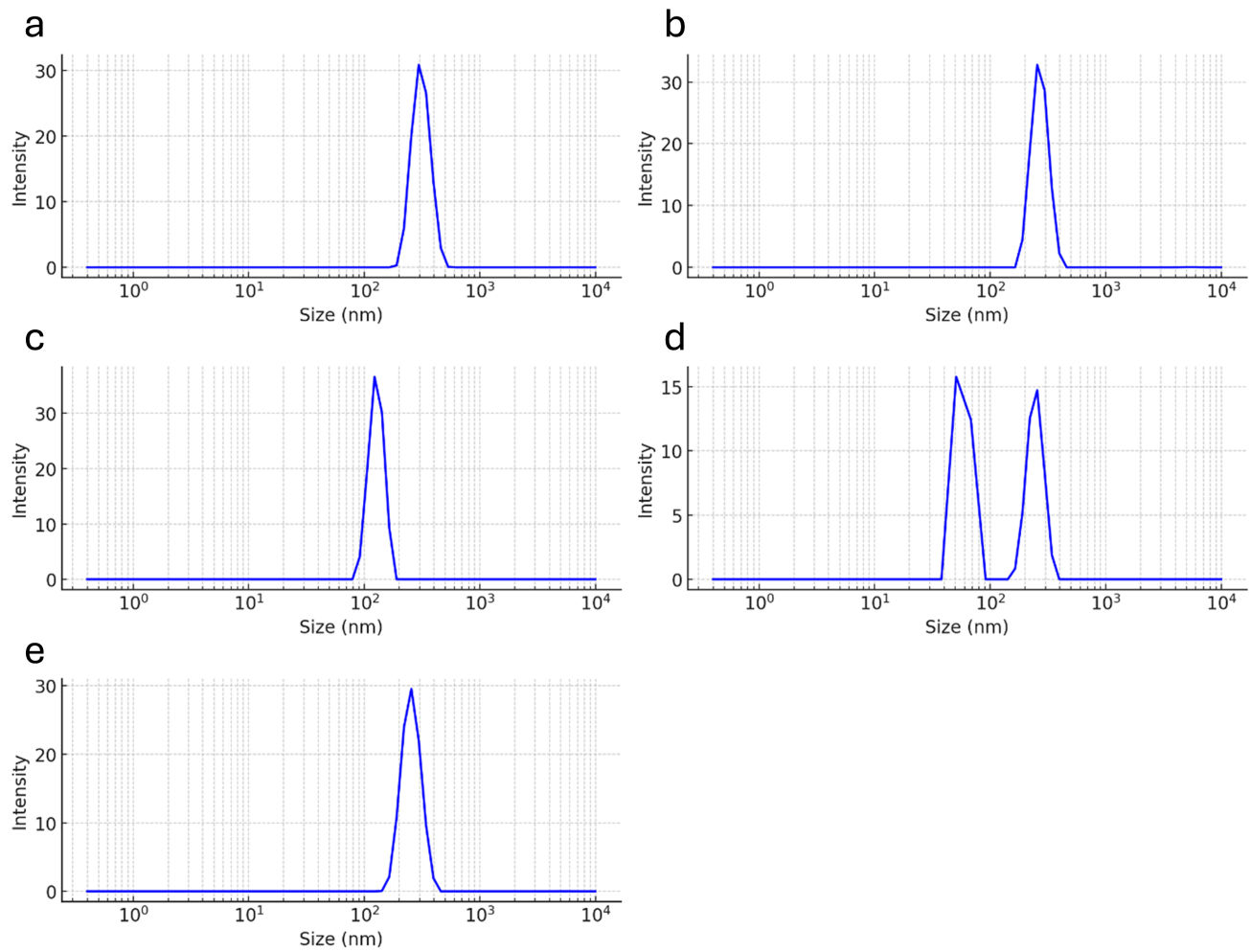


Figure 11: Particle-size distribution resulting from DLS of experimental synthesis a)Sample_21; b)Sample_22; c)Sample_23; d)Sample_24; e)Sample_25.

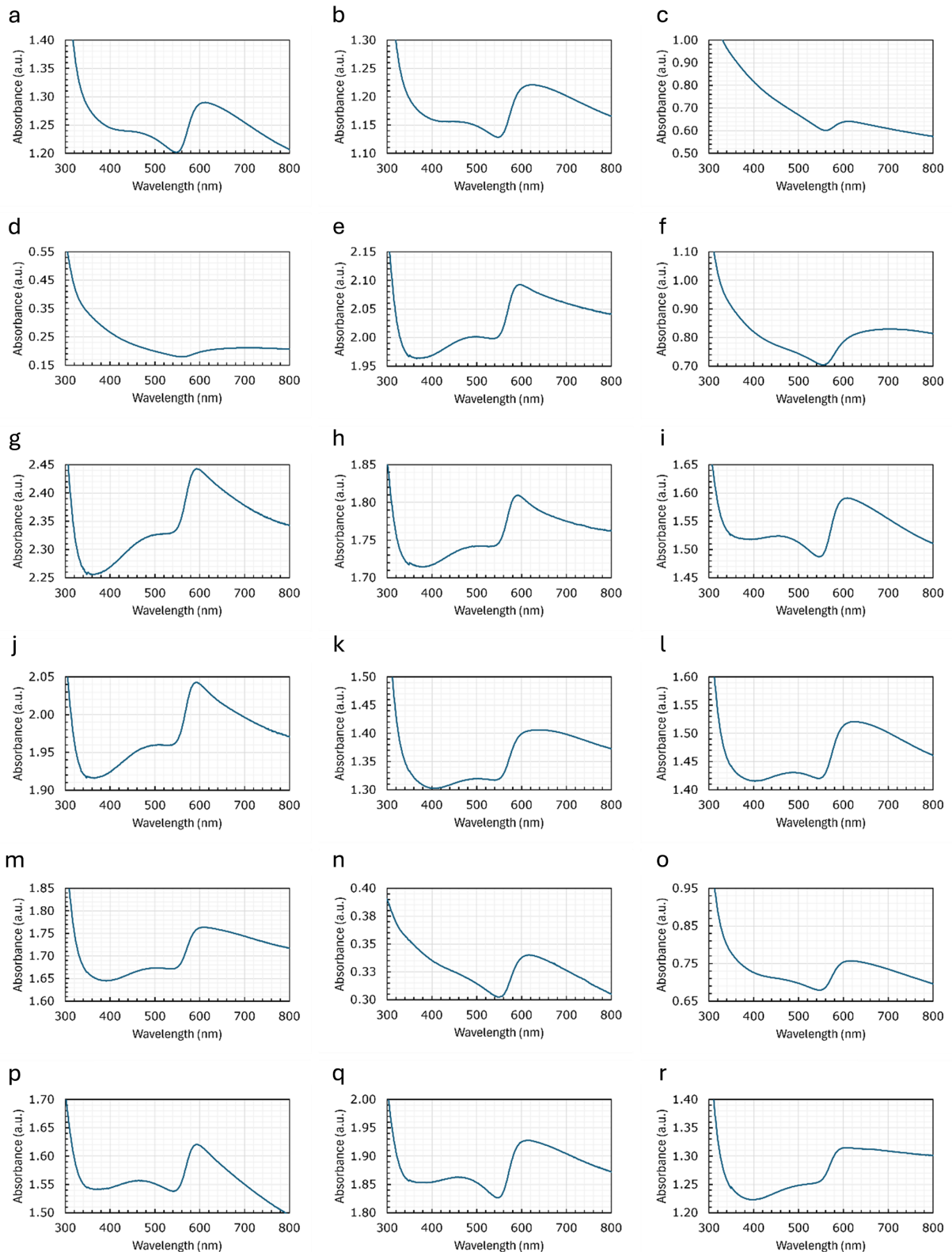


Figure 12: UV-Vis spectra of a) Sample_1; b) Sample_2; c) Sample_3; d) Sample_4; e) Sample_5; f) Sample_6; g) Sample_7; h) Sample_8; i) Sample_9; j) Sample_10; k) Sample_11; l) Sample_12; m) Sample_13; n) Sample_14; o) Sample_15; p) Sample_16; q) Sample_17; r) Sample_18.

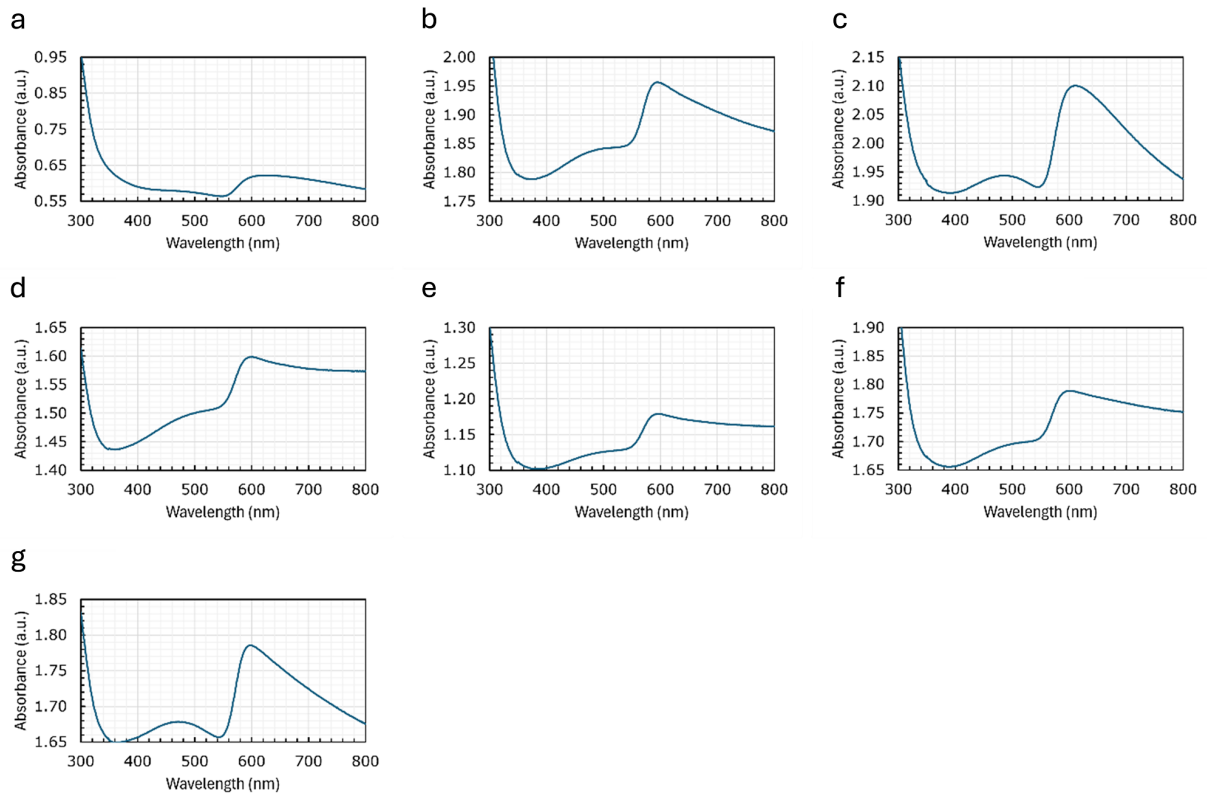


Figure 13: UV-Vis spectra of a) Sample_19; b) Sample_20; c) Sample_21; d) Sample_22; e) Sample_23; f) Sample_24; g) Sample_25.

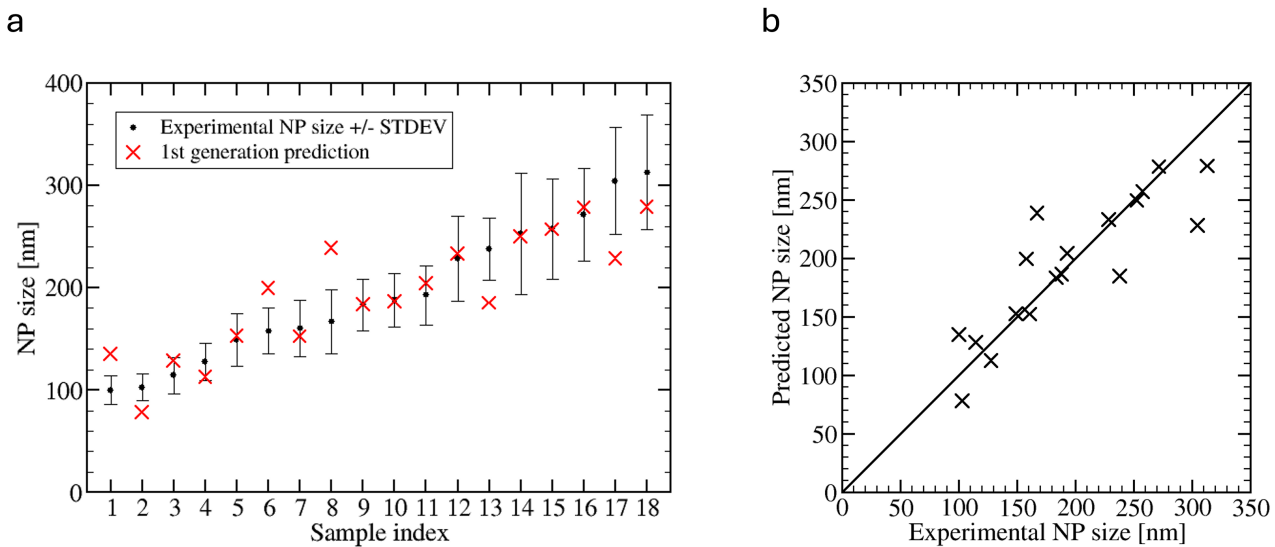


Figure 14: a) Plot of the experimentally measured particle size and their standard deviation in ascending order (black) with the corresponding predicted particle size of the second generation ensemble model (red); b) Parity plot of the actual, experimental size against the corresponding predicted size using the first generation ensemble model.

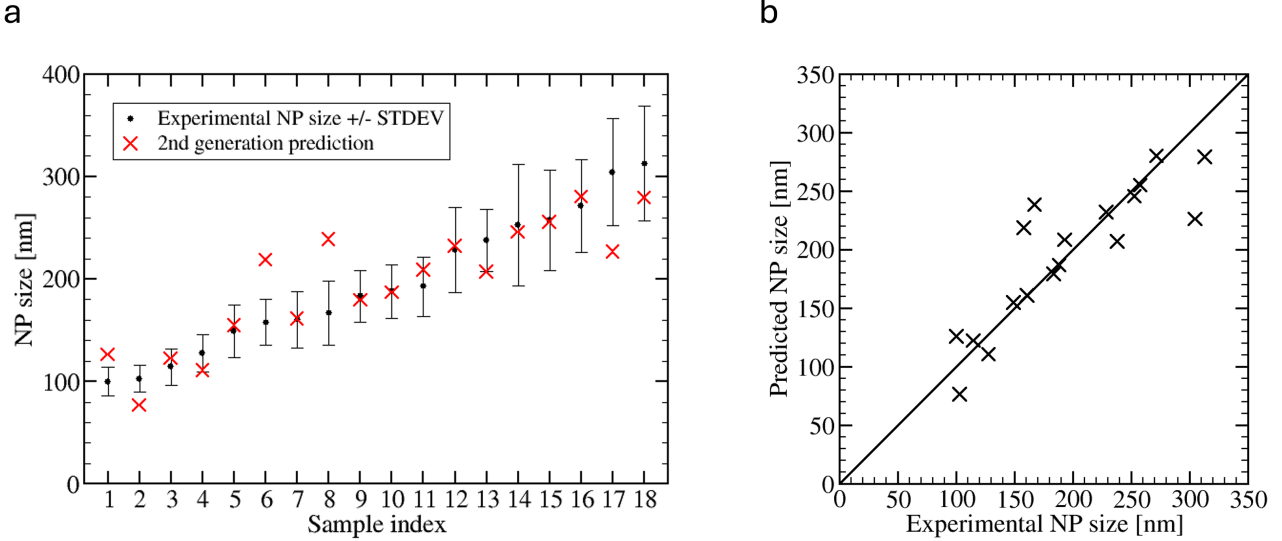


Figure 15: a) Plot of the experimentally measured particle size and their standard deviation in ascending order (black) with the corresponding predicted particle size of the second generation ensemble model (red); b) Parity plot of the actual, experimental size against the corresponding predicted size using the second generation ensemble model.

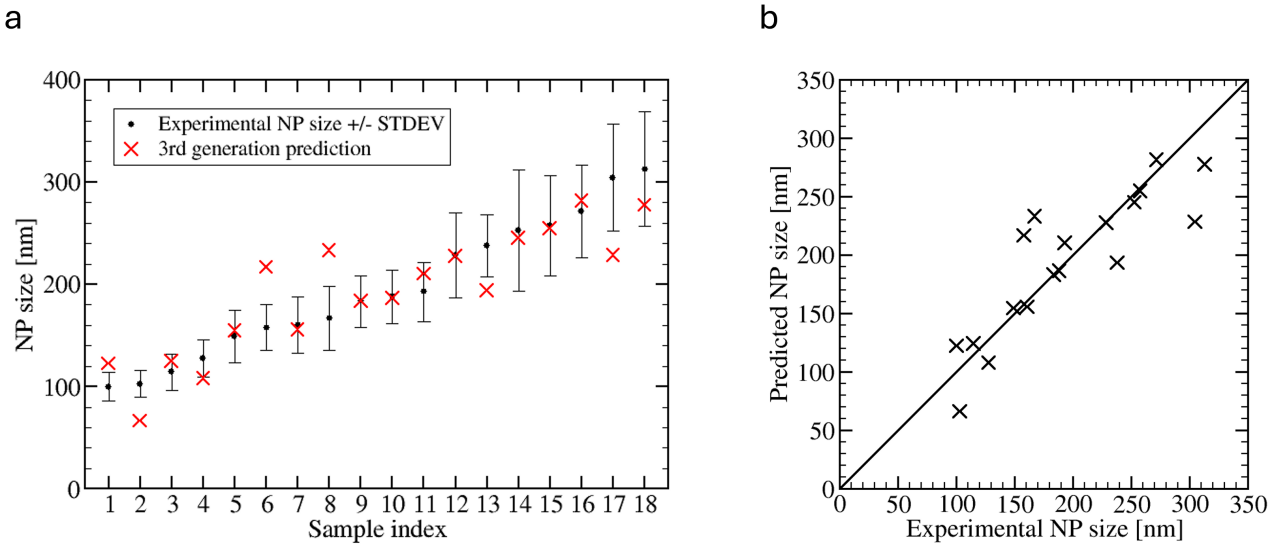


Figure 16: a) Plot of the experimentally measured particle size and their standard deviation in ascending order (black) with the corresponding predicted particle size of the third generation ensemble model (red); b) Parity plot of the actual, experimental size against the corresponding predicted size using the third generation ensemble model.